Photon-assisted electronic and spin transport through two T-shaped three-quantum-dot molecules embedded in an Aharonov–Bohm interferometer*

Jiyuan Bai(白继元)[1,3], Li Li(李立)[1,†], Zelong He(贺泽龙)[2,‡], Shujiang Ye(叶树江)[3], Shujun Zhao(赵树军)[3], Suihu Dang(党随虎)[2], and Weimin Sun(孙伟民)[1]

[1] *Key Laboratory of In-fiber Integrated Optics of Ministry of Education, College of Science, Harbin Engineering University, Harbin* 150001, *China*
[2] *School of Electronic and Information Engineering, Yangtze Normal University, Chongqing* 408003, *China*
[3] *School of Electrical and Information Engineering, Heilongjiang Institute of Technology, Harbin* 150050, *China*

(Received 29 June 2017; revised manuscript received 7 August 2017; published online 30 September 2017)

We investigate the time-modulated electronic and spin transport properties through two T-shaped three-quantum-dot molecules embedded in an Aharonov–Bohm (A–B) interferometer. By using the Keldysh non-equilibrium Green's function technique, the photon-assisted spin-dependent average current is analyzed. The T-shaped three-quantum-dot molecule A–B interferometer exhibits excellent controllability in the average current resonance spectra by adjusting the interdot coupling strength, Rashba spin–orbit coupling strength, magnetic flux, and amplitude of the time-dependent external field. Efficient spin filtering and multiple electron-photon pump functions are exploited in the multi-quantum-dot molecule A–B interferometer by a time-modulated external field.

Keywords: non-equilibrium Green's function, photon-assisted electron transport, Aharonov–Bohm interferometer, Rashba spin–orbit coupling

PACS: 73.63.–b, 73.23.–b, 05.60.Gg **DOI:** 10.1088/1674-1056/26/11/117302

1. Introduction

Spintronics of the quantum dot system has aroused a great deal of interest for its application in spin functional device and quantum computing.[1–7] Quantum computing schemes based on spin in quantum dots have been proposed.[4,5] Many of the elements necessary for quantum computation have been realized experimentally.[6] It is expected that the quantum dot device will be used as an integrated quantum chip in the future.[7]

Multiple quantum dots can be coupled to form an artificial molecule for versatile important transport phenomena including the quantum interference,[8–12] the quantum Hall effect,[13,14] the Kondo effect,[15–17] the thermoelectric effect,[18,19] and the Fano effect.[20–23] Particularly, the photon-assisted tunneling effect in the quantum dot system has been surprisingly observed.[24,25] Photon-assisted tunneling enables the electron to reach a previously inaccessible energy state by absorbing or emitting photons from a microwave signal.[26] Coherent molecular states in the coupled quantum dots can be probed through photon-assisted tunneling.[27] The photon-assisted sidebands originating from the ground state and the excited state can be obtained using the nonequilibrium Green's function approach,[28] which gives good agreement with the experiment.[29] Ground state resonance and photon-induced excited state resonance have been found to arise from terahertz photon-assisted tunneling in a single self-assembled InAs quantum dot.[30] The photon-assisted tunneling effect offers a useful way to study the coherent properties of a charge qubit formed in an undoped GaAs/AlGaAs heterostructure.[31] The photon-assisted shot noise induced by the time-dependent fields has been investigated to reveal some significant results for spintronics.[32–34] The electron pump has been proposed in a double quantum dot system by using an asymmetric time-dependent external field.[35,36]

Various mesoscopic single/double-quantum dot devices have been presented for quantum molecular effect and quantum information application, aiming at exploiting the nanospintronic functionality. In recent years, a great deal of attention has been paid to the three-quantum-dot structure, which can achieve all the physical features of single- and double-quantum-dot systems. In addition, some novel transport characteristics that do not present in the single- or double-quantum dot can be obtained. They also provide the possibility to manipulate each of the quantum dots separately

*Project supported by the National Natural Science Foundation of China (Grant Nos. 11447132 and 11504042), the Natural Science Foundation of Heilongjiang, China (Grant No. A201405), 111 Project to Harbin Engineering University, China (Grant No. B13015), Chongqing Science and Technology Commission Project, China (Grant Nos. cstc2014jcyjA00032 and cstc2016jcyjA1158), and Scientific Research Project for Advanced Talents of Yangtze Normal University, China (Grant No. 2017KYQD09).

†Corresponding author. E-mail: lylee_heu@hrbeu.edu.cn
‡Corresponding author. E-mail: hrbhzl@126.com

© 2017 Chinese Physical Society and IOP Publishing Ltd

and enlarges the dimension of parameter space for transport properties. Three-quantum-dot structures are capable of deducing to multiply-quantum-dot systems. In this paper, we construct a T-shaped three-quantum-dot molecule A–B interferometer. The time-modulated quantum transport properties are focused on the action of a time-dependent external field. Utilizing the Keldysh non-equilibrium Green's function method,[37,38] we conduct an analytical and numerical study of the photon-assisted electronic and spin transport characteristics. The extended structure of the T-shaped three-quantum-dot molecule A–B interferometer exhibits excellent controllability in the average current by adjusting the interdot coupling strength, Rashba spin–orbit coupling strength, magnetic flux, and amplitude of the time-dependent AC field. Efficient spin filtering and multiple electron-photon pump functions are exploited in a multi-quantum-dot A–B interferometer by the time-modulated external field.

2. Model and method

Two T-shaped three-quantum-dot molecules are embedded in the two arms of the A–B interferometer, respectively. As shown in Fig. 1, quantum dots 1 and 2 are directly coupled with the leads. The single spin-degeneracy energy level in each dot is relevant. For insight into the essential features of the time-modulated quantum transport properties, the interdot and intradot electron–electron interactions are negligible in the composite system of the multi-quantum-dot molecule A–B interferometer. The DC bias voltage $V_{\rm DC}$ is applied to the two terminals of the A–B interferometer with time-dependent fields $W_{\rm L}(t) = W_{\rm L}\cos(\omega t)$, $W_{\rm R}(t) = W_{\rm R}\cos(\omega t)$, and $W_{\rm D}(t) = W_{\rm D}\cos(\omega t)$. The subscripts L, R, and D represent the left lead, the right lead, and the quantum dot, respectively; $W_{\rm L(R,D)}$ and ω are the amplitude and frequency of the time-dependent field, respectively.

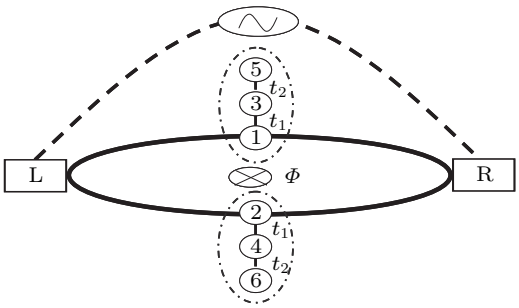


Fig. 1. Schematic of a T-shaped three-quantum-dot molecule A–B interferometer.

The Hamiltonian of the whole system can be written as

$$H = \sum_{\beta={\rm L,R}} H_\beta + H_{\rm D} + H_{\rm T}. \tag{1}$$

The term H_β describes the leads under the non-interacting quasiparticle approximation

$$H_\beta = \sum_{k,\sigma} \varepsilon_{k_\beta}(t) c^+_{k_\beta\sigma} c_{k_\beta\sigma}, \tag{2}$$

where the electron energy $\varepsilon_{k_\beta}(t) = \varepsilon^0_{k_\beta} + eV - eW_\beta(t) = \varepsilon^0_{k_\beta} + eV - eW_\beta\cos(\omega t)$. The electron energy includes the photon-assisted contribution of the time-dependent field interacting with the electrons. $\beta(={\rm L,R})$ represent the left and right leads; $c^+_{k_\beta\sigma}(c_{k_\beta\sigma})$ is the creation (annihilation) operator for electrons in lead β with spin index σ; and k represents the wave vector.

In Eq. (1), $H_{\rm D}$ describes the two three-quantum-dot molecules

$$\begin{aligned} H_{\rm D} = & \sum_{\sigma,j=1,2,3,4,5,6} \varepsilon_{j\sigma}(t) d^+_{j\sigma} d_{j\sigma} - (t_1 d^+_{1\sigma} d_{3\sigma} + t_2 d^+_{3\sigma} d_{5\sigma} \\ & + t_1 d^+_{2\sigma} d_{4\sigma} + t_2 d^+_{4\sigma} d_{6\sigma} + {\rm H.C.}), \end{aligned} \tag{3}$$

where $d^+_{j\sigma}(d_{j\sigma})$ is the creation (annihilation) operator with quantum dot energy $\varepsilon_{jd}(t) = \varepsilon^0_j - eW_{\rm D}\cos(\omega t)$, ε^0_j is the single particle energy in the j-th quantum dot, and $t_{1(2)}$ is the tunneling coupling strength between the quantum dots in the T-shaped three-quantum-dot molecule.

The last term $H_{\rm T}$ on the right-hand side of Eq. (1) describes the dot-lead tunneling

$$H_{\rm T} = \sum_{k\sigma} \sum_{\beta={\rm L,R}} (t_{1\sigma\beta} c^+_{k\beta\sigma} d_{1\sigma} + t_{2\sigma\beta} c^+_{k\beta\sigma} d_{2\sigma} + {\rm H.C.}), \tag{4}$$

where $t_{1\sigma\beta}(t_{2\sigma\beta})$ indicates the k-independent coupling between the lead $\beta$and quantum dot 1 (2). By taking into account the Rashba spin–orbit coupling and the magnetic flux,[39,40] the tunnel matrix elements $t_{1\sigma\beta}$ and $t_{2\sigma\beta}$ are written as $t_{1\sigma{\rm L}} = |t_{1{\rm L}}|\,{\rm e}^{{\rm i}(\psi/4-\sigma\varphi_{\rm R1}/2)}$, $t_{2\sigma{\rm L}} = |t_{2{\rm L}}|\,{\rm e}^{-{\rm i}(\psi/4+\sigma\varphi_{\rm R2}/2)}$, $t_{1\sigma R} = |t_{1{\rm R}}|\,{\rm e}^{-({\rm i}\psi/4-\sigma\varphi_{\rm R1}/2)}$, and $t_{2\sigma{\rm R}} = |t_{2{\rm R}}|\,{\rm e}^{{\rm i}(\psi/4+\sigma\varphi_{\rm R2}/2)}$, where $\phi_{\rm R1(R2)}$ denotes the spin–orbit-coupling-induced Rashba phase factor in the quantum dot 1 (2), and ψ is the magnetic flux-induced phase factor.

In the wide-band limit, the relationship between the retarded self-energy and the linewidth function is given by[4]

$$\Sigma^{\rm r}_{\beta\sigma}(t,t') = -\frac{\rm i}{2}\delta(t-t')\Gamma^\beta_\sigma, \tag{5}$$

where $\Gamma^\beta_{ll'\sigma}(\varepsilon,t,t') = 2\pi\rho_\beta t_{l\sigma\beta} t^*_{l'\sigma\beta}\,{\rm e}^{{\rm i}\int^{t'}_{t} W_\beta(\tau)\,{\rm d}\tau}$, and ρ_β is the spin density of states in the β leads. The matrix Γ^β_σ can be written as

$$\Gamma_{\sigma}^{\mathrm{L(R)}}=\begin{pmatrix} \Gamma_1^{\mathrm{L(R)}} & \sqrt{\Gamma_1^{\mathrm{L(R)}}\Gamma_2^{\mathrm{L(R)}}}\,\mathrm{e}^{\pm\mathrm{i}(\psi-\sigma\Delta\varphi_{\mathrm{R}})/2} & 0 & 0 & 0 & 0 \\ \sqrt{\Gamma_1^{\mathrm{L(R)}}\Gamma_2^{\mathrm{L(R)}}}\,\mathrm{e}^{\mp\mathrm{i}(\psi-\sigma\Delta\varphi_{\mathrm{R}})/2} & \Gamma_2^{\mathrm{L(R)}} & 0 & 0 & 0 & 0 \\ 0 & 0 & 0 & 0 & 0 & 0 \\ 0 & 0 & 0 & 0 & 0 & 0 \\ 0 & 0 & 0 & 0 & 0 & 0 \\ 0 & 0 & 0 & 0 & 0 & 0 \end{pmatrix}, \tag{6}$$

in which Γ_l^{β} is short for Γ_{ll}^{β}, and the phase factor $\Delta\phi_{\mathrm{R}}=\phi_{\mathrm{R1}}-\phi_{\mathrm{R2}}$.

The time-dependent transient current $I(t)$ is determined by[35,36]

$$I_{\beta\sigma}(t)=-\frac{2e}{\hbar}\,\mathrm{Im}\int_{-\infty}^{t}\mathrm{d}t'\int\frac{\mathrm{d}\varepsilon}{2\pi}\,\mathrm{Tr}\left\{\mathrm{e}^{-\mathrm{i}\varepsilon(t'-t)}\Gamma_{\sigma}^{\beta}(\varepsilon,t,t')\times\left[G_{\sigma}^{<}(t,t')+f_{\beta}(\varepsilon)G_{\sigma}^{\mathrm{r}}(t,t')\right]\right\}, \tag{7}$$

where $f_{\beta}(\varepsilon)=\left\{1+\exp\left[(\varepsilon-\mu_{\beta})/k_{\mathrm{B}}T\right]\right\}^{-1}$ is the Fermi distribution function, $\mu_{\mathrm{L}}=-\mu_{\mathrm{R}}=V/2$, and V is a DC bias between the left and right leads. The retarded Green's function G^{r} is obtained by the Dyson equation

$$G_{\sigma}^{\mathrm{r}}(t,t')=\int\frac{\mathrm{d}\varepsilon}{2\pi}\exp\left[-\mathrm{i}\varepsilon(t-t')-\mathrm{i}\int_{t'}^{t}\mathrm{d}\tau W_{\mathrm{D}}\cos(\omega\tau)\right]G_{\sigma}^{\mathrm{r}}(\varepsilon), \tag{8}$$

$$G_{\sigma}^{\mathrm{r}}(\varepsilon)=\left\{\left[g_{\sigma}^{\mathrm{r}}(\varepsilon)\right]^{-1}-\Sigma_{\sigma}^{\mathrm{r}}(\varepsilon)\right\}^{-1}, \tag{9}$$

where $g_{\sigma}^{\mathrm{r}}(\varepsilon)$ is the Fourier transform of $g_{jj}^{\mathrm{r}}(t,t')=-\mathrm{i}\theta(t-t')\exp\left[-\mathrm{i}\int_{t'}^{t}\varepsilon_j(t_1)\,\mathrm{d}t_1\right]$. The lesser Green's function is $G^{<}=G^{\mathrm{r}}\Sigma^{<}G^{\mathrm{a}}$, where $G^{\mathrm{a}}=(G^{\mathrm{r}})^{+}$. The Green's function G^{r} can be calculated by the equations of motion for each Green's function

$$G^{\mathrm{r}}(\varepsilon)=\begin{pmatrix} \varepsilon-\varepsilon_1-\frac{\mathrm{i}}{2}\left(\Gamma_{11}^{\mathrm{L}}+\Gamma_{11}^{\mathrm{R}}\right) & \frac{\mathrm{i}}{2}\left(\Gamma_{12}^{\mathrm{L}}+\Gamma_{12}^{\mathrm{R}}\right) & t_1 & 0 & 0 & 0 \\ \frac{\mathrm{i}}{2}\left(\Gamma_{21}^{\mathrm{L}}+\Gamma_{21}^{\mathrm{R}}\right) & \varepsilon-\varepsilon_2-\frac{\mathrm{i}}{2}\left(\Gamma_{22}^{\mathrm{L}}+\Gamma_{22}^{\mathrm{R}}\right) & 0 & t_1 & 0 & 0 \\ t_1 & 0 & \varepsilon-\varepsilon_3 & 0 & t_2 & 0 \\ 0 & t_1 & 0 & \varepsilon-\varepsilon_4 & 0 & t_2 \\ 0 & 0 & t_2 & 0 & \varepsilon-\varepsilon_5 & 0 \\ 0 & 0 & 0 & t_2 & 0 & \varepsilon-\varepsilon_6 \end{pmatrix}^{-1}. \tag{10}$$

Substituting formulas (8) and (9) into Eq. (7), the time-dependent transient current is derived as

$$I_{\beta\sigma}(t)=-\frac{e}{\hbar}\int\frac{\mathrm{d}\varepsilon}{2\pi}\,\mathrm{Tr}\,\mathrm{Im}\left\{2f_{\beta}(\varepsilon)\Gamma_{\sigma}^{\beta}A_{\beta\sigma}(\varepsilon,t)+\mathrm{i}\Gamma_{\sigma}^{\beta}\sum_{\alpha=\mathrm{L,R}}f_{\alpha}(\varepsilon)A_{\alpha\sigma}(\varepsilon,t)\Gamma_{\sigma}^{\sigma}A_{\alpha\sigma}^{+}(\varepsilon,t)\right\}, \tag{11}$$

where

$$A_{\beta\sigma}(\varepsilon,t)=\exp\left[\frac{\mathrm{i}e\left(W_{\beta}-W_{\mathrm{D}}\right)\sin(\omega t)}{\omega}\right]\times\sum_{n}J_n\left(\frac{W_{\mathrm{D}}-W_{\beta}}{\omega}\right)\mathrm{e}^{\mathrm{i}n\omega t}G_{\sigma}^{\mathrm{r}}(\varepsilon_n). \tag{12}$$

In Eq. (12), J_n is the first kind of Bessel function and $\varepsilon_n=\varepsilon-n\omega$. Thereby, the instantaneous current $I_{\beta\sigma}(t)$ can be calculated by numerically resolving Eq. (11) . Consequently, the time-averaged current of $I_{\beta\sigma}(t)$ is evaluated by

$$\langle I\rangle=\frac{2e}{\hbar}\int\frac{\mathrm{d}\varepsilon}{2\pi}\sum_{n}\mathrm{Tr}\left\{\left[J_n^2\left(\frac{W_{\mathrm{D}}-W_{\mathrm{L}}}{\omega}\right)f_{\mathrm{L}}(\varepsilon)-J_n^2\left(\frac{W_{\mathrm{D}}-W_{\mathrm{R}}}{\omega}\right)f_{\mathrm{R}}(\varepsilon)\right]\Gamma_{\sigma}^{\mathrm{L}}G_{\sigma}^{\mathrm{r}}(\varepsilon_n)\Gamma_{\sigma}^{\mathrm{R}}G_{\sigma}^{\mathrm{a}}(\varepsilon_n)\right\}. \tag{13}$$

3. Numerical results and discussion

In this section, we present the time-modulated quantum transport properties of the three-quantum-dot molecule A–B interferometer. The characteristics of the photon-assisted spin-dependent average current are numerically simulated. The DC bias voltage is set to $V=0.05$, the temperature is $k_{\mathrm{B}}T=0.001$, and the dot-lead coupling strength is $\Gamma_1^{\beta}=\Gamma_2^{\beta}=0.2\Gamma$, taking Γ as the unit of energy. The inter-dot coupling strength is $t_1=t_2=t$, the quantum dot energy $\varepsilon_{1(2,3,4,5,6)}=\varepsilon_{\mathrm{d}}$, $\hbar=1$, and $e=1$. On the basis of the physical model and formalism in Section 2, we implement the rigorous numerical simulations as shown in Figs. 2–8.

Figure 2 shows the average current spectra versus quantum dot energy at various amplitudes of the time-dependent external field in the absence of magnetic flux and Rashba spin–orbit coupling. The interdot coupling strength is taken as $t=\sqrt{2}k/2$. Correspondingly, the main peaks of the average current appear at $\varepsilon_{\mathrm{d}}=0,\pm k$. The physical parameters are typically taken as $k=2.0$, $\omega=1.0$, $\Delta\phi_{\mathrm{R}}=0$, and $\psi=0$.

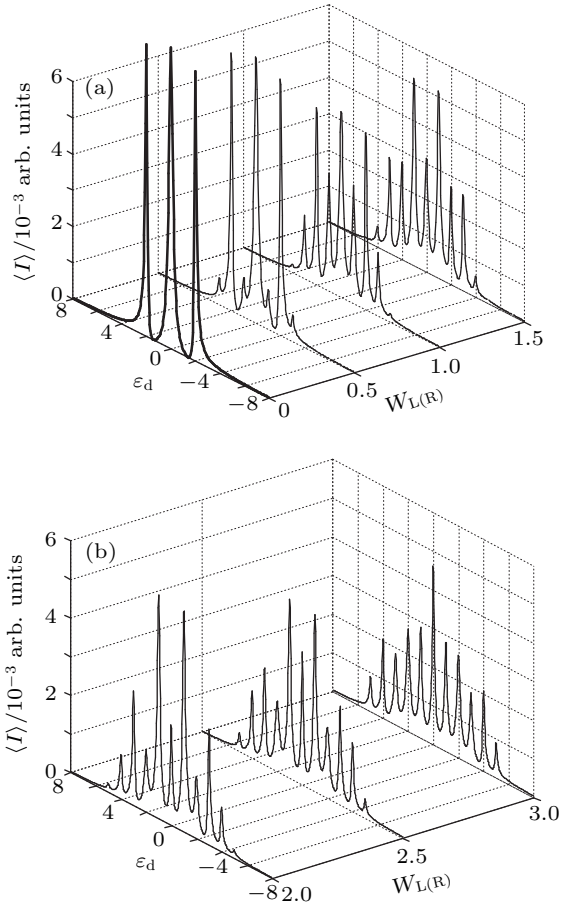


Fig. 2. Average current spectra versus quantum dot energy at various amplitudes of the symmetrical time-dependent field. For clear indication of the spectra evolution, the range of the field amplitude $W_{L(R)}$ covers (a) 0 to 1.5 and (b) 2 to 3 in the subfigures. The typical parameters are $k = 2$, $\omega = 1.0$, $\Delta\phi_R = 0$, and $\psi = 0$.

In Fig. 2(a), the average current of the system without applying a time-dependent external field is shown by the thick solid line. Only three average current peaks at $\varepsilon_d = 0, \pm k$ appear in such a six quantum dots structure. Two T-shaped triple-quantum dot molecules are completely equivalent, which leads to the degeneration of the energy levels.

Further introducing a time-dependent external field, we calculate the time-averaged current of the triple-quantum dot molecule A–B interferometer. The external field is applied symmetrically to the leads, which is equivalent to applying the external field directly to the quantum dots;[36] thus $W_D = 0$ is valid. As shown in Figs. 2(a) and 2(b), the average current spectra under the time-modulated external field show a remarkable sideband effect. There are a series of resonance peaks in the spectra. The gap between adjacent resonance peaks corresponds to the photon energy of $\hbar\omega$. As the time-dependent field intensity increases, the amplitudes of the three main peaks become smaller. After the external field exceeds a threshold, the peak amplitudes increase with the increasing external field. In the mean time, the sideband peaks in the average current spectra exhibit an anti-phase behavior in comparison with the three main resonance peaks. The sideband peaks first go upwards and then downwards back with the increase of the external field, as shown in Figs. 2(a) and 2(b). This is because the height of the n-th peak is determined by the Bessel function $J_n^2\left(W_\beta/\omega\right)$, which derives from the action of the time-dependent external field. In addition, one can find that the summation of the heights of all peaks equals to that of the original three main resonance peaks. This result can be explained by whether the tunneling electron can absorb or emit one or several photons.

By tuning the symmetrical time-modulated external field, figure 3 shows the dynamics of the average current resonant peaks at $\varepsilon_d = 0, \pm 2$ (the main quantum dot energies), $\varepsilon_d = \pm 1$, ± 3 (the single photon sideband energy levels), and $\varepsilon_d = \pm 4$ (the double photon sideband energy levels). The oscillation effect is revealed for both the main resonant peaks and the sideband peaks. It is closely associated with the contribution of the Bessel function to the transient current response of the triple-quantum dot molecule A–B interferometer. Two fundamental resonant spectra at the intrinsic quantum dot energies of $\varepsilon_d = 2$ and $\varepsilon_d = -2$ have the same oscillation mode (the thick dashed line in Fig. 3). For the dominant resonant peak at zero quantum dot energy, the oscillation mode of $\varepsilon_d = 0$ keeps stronger than that of $\varepsilon_d = \pm 2$, regardless of the symmetric time-modulated field strength. Moreover, the oscillation mode at $\varepsilon_d = 0$ is in phase with that at $\varepsilon_d = \pm 2$. In contrast, as shown in Fig. 3, the single photon sideband peaks at both $\varepsilon_d = \pm 1$ and $\varepsilon_d = \pm 3$ exhibit distinct oscillation modes with opposite phase from the main peaks at $\varepsilon_d = 0$ and $\varepsilon_d = \pm 2$. The double photon sideband peaks at $\varepsilon_d = \pm 4$ also oscillate out of phase with the main oscillation mode of $\varepsilon_d = 0, \pm 2$. The results definitely reflect the different phases of the electron wave functions at different quantum dot energies. By modulating the symmetric external field, the spectra switching of the average current can be implemented by virtue of the electron wave functions at the intrinsic quantum dot energies.

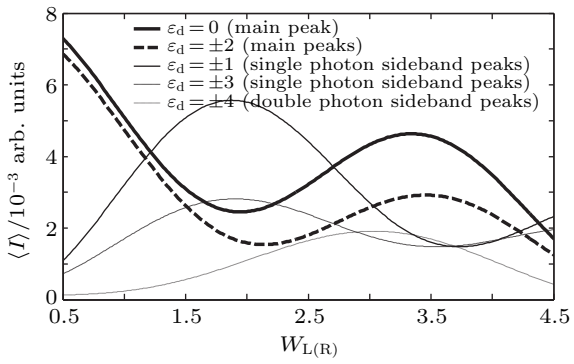


Fig. 3. The oscillation dynamics of the average current resonant peaks at the intrinsic quantum dot energies by tuning the symmetrical time-dependent external field.

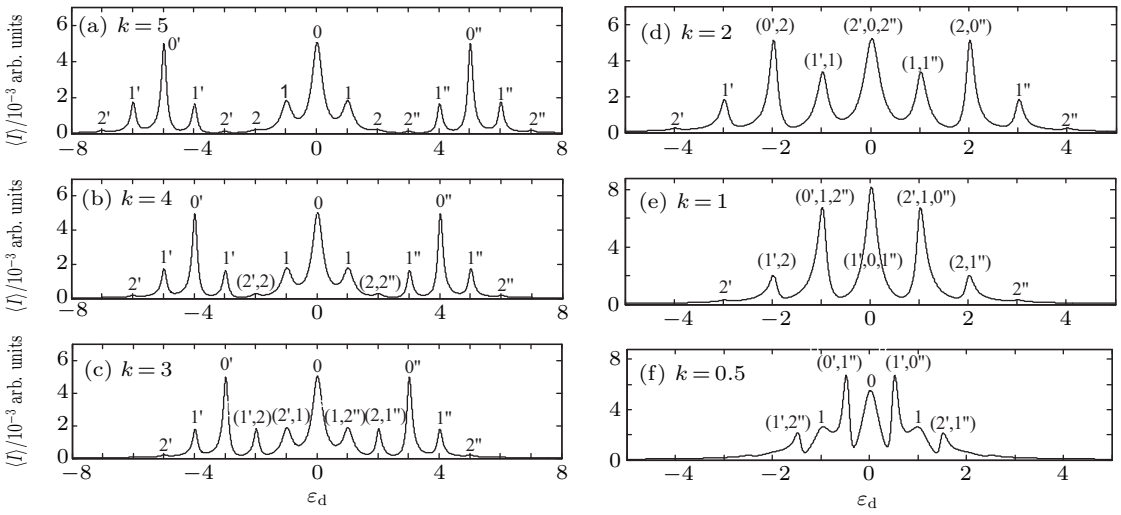


Fig. 4. Average current spectra versus quantum dot energy under various interdot coupling strengths of $k = 0.5$, 1, 2, 3, 4, 5 with a symmetrical time-dependent external field applied. The typical parameters are $W_L = W_R = 1.0$, $\omega = 1.0$, $\Delta\phi_R = 0$, and $\psi = 0$.

The effect of interdot coupling on the average current spectra is shown in Fig. 4, with a symmetrical time-dependent external field applied. The resonant peaks are marked with numbers for clarification. The labels of $0\,(0',0'')$, $1\,(1',1'')$, and $2\,(2',2'')$ indicate the middle (left, right) main peaks, the corresponding single-photon sideband peaks, and the double-photon sideband peaks, respectively. As shown in Fig. 4, the middle main peak marked 0 locates at the energy level of $\varepsilon_d = 0$. The left and right main peaks marked $0'$ and $0''$ always locate at the energy levels of $\varepsilon_d = \pm k$, respectively. With the decrease of the interdot coupling strength, the left and right main peaks $0'0''$ move close to the middle main peak. Meanwhile, the single- and double-photon sideband peaks marked $(1', 1'')$ and $(2', 2'')$ approach to the zero energy level of $\varepsilon_d = 0$. This results in multiple peak overlapping of the main and sideband peaks, as illustrated in Figs. 4(b)–4(f). However, the average current degeneracy is removed completely once the interdot coupling strength becomes strong enough (e.g., $k = 5.0$ as shown in Fig. 4(a)).

We further discuss the controllability of the degenerate average current by adjusting the interdot coupling strength. At the moderate interdot coupling strength of $k = 4.0$, as shown in Fig. 4(b), the overlapping of the double-photon sideband peaks, $(2, 2')$ and $(2, 2'')$, takes place first at the energy levels of $\varepsilon_d = \pm 2$. With decreasing the interdot coupling strength to $k = 3.0$, as shown in Fig. 4(c), the single- and double-photon sideband peaks overlap each other at the energy levels of $\varepsilon_d = \pm 1, \pm 2$. When $k = 2.0$, the middle main peak overlaps with the two double-photon sideband peaks ($2'$ and $2''$), as shown in Fig. 4(d). This leads to a three-fold degenerate average current at $\varepsilon_d = 0$. Additionally, the left and right main peaks ($0'$ and $0''$) overlap with the double-photon sideband peaks around them. It is noted that the single-photon sideband peak values at $\varepsilon_d = \pm 1$ are twice those at $\varepsilon_d = \pm 3$. It results from the superposition of the two single-photon sideband peaks at $\varepsilon_d = 1\ (-1)$, because an electron with energy $\varepsilon_d = 0\ (-2)$ absorbs one photon while an electron with energy $\varepsilon_d = 2\ (0)$ emits one photon. Under the weak interdot coupling of $k = 1.0$ and $k = 0.5$, as shown in Figs. 4(e) and 4(f), the middle main peak is distinct from the left or right main peaks ($0'$ or $0''$) due to the complex superposition of the main peaks and the single-photon sideband peaks. The overlap state $(1', 0, 1'')$ of the middle main peak with the two single-photon sideband peaks is found in Fig. 4(e). More notably, the left or right main peak ($0'$ or $0''$) overlaps simultaneously with both single- and double-photon sideband peaks. This causes the middle main peak 0 to be greater than the left or right main peak ($0'$ or $0''$). In contrast, figure 4(f) shows that the left (right) main peak and the single-photon sideband peaks marked $1''(1')$ overlap correspondingly to be a degenerate average current peak. However, the overlap effect of the middle main peak (marked 0) is no longer present, which causes the middle main peak amplitude to be smaller than the left (or right) one. Accordingly, the interdot coupling strength is suggested to play a key role affecting the magnitude and position of the average current resonance peaks. Physically, the distance between the quantum dot levels can be varied by adjusting the interdot coupling strength. In the meantime, the locations of the photon-assisted sideband peaks are also changed. Therefore, each current peak comes from the contributions of electrons tunneling through different channels. The electrons from the left lead tunnel to the right lead travel via many different ways: tunneling by absorbing/emitting one photon or two photons, etc. The coherent effect happens because the electron tunneling through different channels may have different phases.

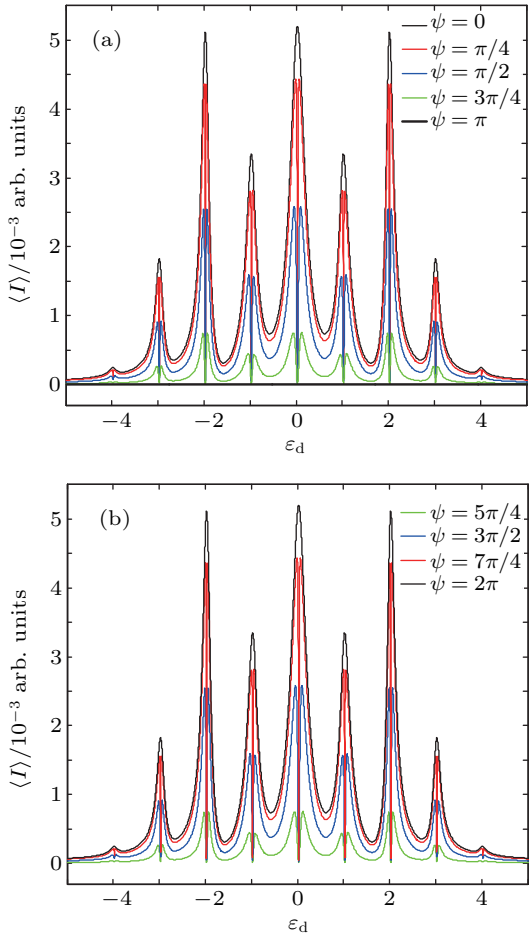


Fig. 5. (color online) Average current resonance spectra versus quantum dot energy under a magnetic flux in the ranges of (a) 0 to π, (b) $5\pi/4$ to 2π, with $k = 2.0$, $W_L = W_R = 1.0$, and $\Delta\phi_R = 0$.

Electron transport properties of the composite device are strongly influenced by the interplay of the quantum interference due to the T-shape arrangement of the three-quantum-dot molecules. Quantum interference governs physically the average current resonance of the model system. The quantum interference can be manipulated by the phase difference of electron wavefunctions between the two branches of the A–B interferometer via a magnetic flux. Figure 5 shows the evolution of the average current resonance spectra by scanning the magnetic flux in the range of 0–2π. Note that the magnetic flux period of the average current resonance is 2π, showing a significant A–B effect of electron transport. Originally without magnetic flux ($\psi = 0$), the intrinsic singlet resonance of the average current occurs exactly at the quantum dot energy levels of $\varepsilon_d = 0, \pm n$ ($n = 1, 2, 3, 4$). The average current maximum implies the maximum number of electrons passing through the two branches of the A–B interferometer. When introducing a magnetic flux into the model device, the prominent modification to the average current resonance is the doublet splitting of the resonance peaks, as shown in Fig. 5. The magnetic flux leads to a phase difference between the electron wavefunctions in the up and down branches, so the interference occurs. The increase of the electron number causes more of a drop for interfere current and max of current becoming minimum, i.e., splitting phenomenon. Each current peak splits into two peaks. Particularly under the magnetic flux of $\psi = \pi$, the completely destructive quantum interference leads to the zero average current spectra without resonance. Under the magnetic flux of $\psi = 2\pi$, the constructive quantum interference takes place completely in phase to reproduce the singlet resonance states in the average current spectra.

Additionally, figure 5(a) illustrates the reduction of the average current resonance amplitudes with increasing magnetic flux in the range of $0 < \psi < \pi$. As the magnetic flux further increases in $\pi < \psi < 2\pi$, the average current resonance recovers gradually, as shown in Fig. 5(b). The simulation results indicate that the average current resonance spectra under $\psi = \pi/4$, $\pi/2$, $3\pi/4$ are the same as those under $\psi = 7\pi/4$, $3\pi/2$, $5\pi/4$, respectively. The 2π-periodic modulation of the average current resonance via the magnetic flux is favorable in practice for tunable quantum devices.

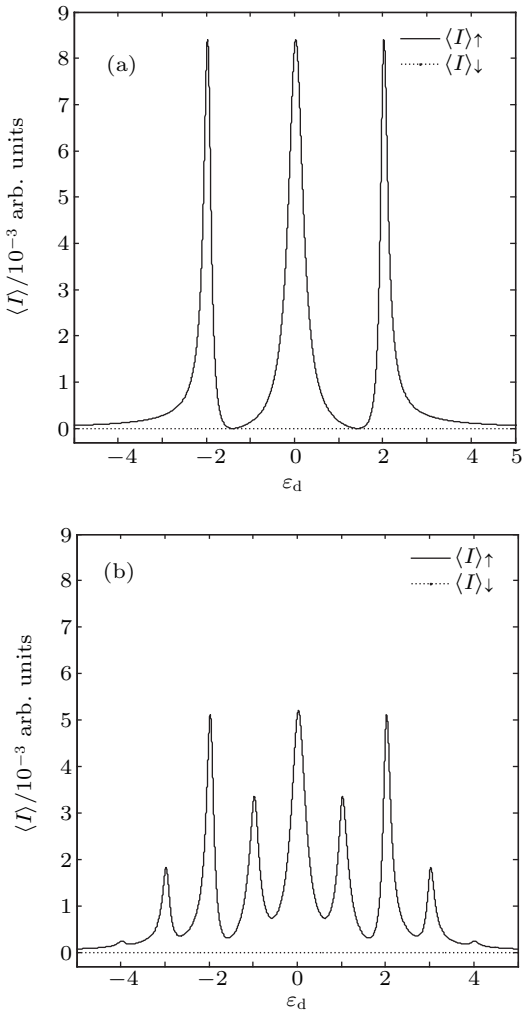


Fig. 6. Spin-dependent average current resonance spectra (a) before and (b) after applying the time-modulated external field, with $k = 2.0$, $W_L = W_R = 1.0$, $\psi = \pi/2$, and $\Delta\phi_R = \pi/2$. The spin up/down is denoted by arrow $\uparrow$ / $\downarrow$.

In the model system, the Rashba spin–orbit-coupling-induced phase factor ϕ_R is determined by $\phi_R = \alpha L_i m^*/\hbar^2$ according to Refs. [39]–[43], where α is the Rashba spin–orbit coupling strength, m^* is the effective mass of electron, and L_i is the length of quantum dot i. The Rashba spin–orbit coupling strength is about 3×10^{-11} eVm in semiconductors. The phase factor ϕ_R is adjustable by varying the strength of the electric field applied in the experiment, as presented in Refs. [41]–[43].

In Fig. 6, we show the simulated spin-dependent average current resonance spectra, taking into account the time-modulated external field and magnetic flux. Here we emphasize the role of the Rashba spin–orbit-coupling induced phase factor. $\langle I\rangle_\uparrow$ (solid line) and $\langle I\rangle_\downarrow$ (dotted line) represent the spin up and spin down average currents, respectively. Figure 6(a) shows the spin-dependent average current spectra before applying the external field. For spin up electrons (spin index $\sigma = 1$), when the magnetic flux satisfies $\psi = \Delta\phi_R$, one has $\psi - \sigma\Delta\phi_R = 0$. The phase factors induced by the Rashba spin–orbit coupling and magnetic flux cancel each other out. This causes the spin up average current to degenerate into the original one with three resonance peaks shown in Fig. 2(a). Two anti-resonance zero dips exist at $\varepsilon_d = \pm\sqrt{2}$. In contrast, for spin down electrons (spin index $\sigma = -1$), one has $\psi - \sigma\Delta\phi_R = \pi$. The half-wave phase difference of the electron wavefunctions through the A–B interferometer leads to a completely destructive quantum interference. It results in zero average current response. This forbids the spin down polarized transmission of electrons.

Figure 6(b) shows the spin-dependent average current spectra after introducing the time-modulated external field. For spin up electrons, the photon-modified sideband resonance peaks emerge noticeably in the average current spectra. Meanwhile the anti-resonance dips at $\varepsilon_d = \pm\sqrt{2}$ are all beyond zero-level. This implies that the spin up electrons with energy $\varepsilon_d = \pm\sqrt{2}$ have an anti-resonance tunneling effect under the time-modulated external field. For spin down electrons, the time-modulated external field does not affect the destructive quantum interference resulting in zero average current. It is suggested, as shown in Fig. 6(b), that the pure spin up polarized transmission is obtainable in the whole quantum dot energy region under the time-modulated external field. Note that when the induced phase factor is $\Delta\phi_R = -\pi/2$, the spin-dependent average current resonance spectra are correspondingly interchanged for spin up/down electrons in Fig. 6. The pure spin down polarized transmission occurs. Now the advancement in experiments and theories indicates that the tuning of the Rashba spin–orbit coupling strength is executable in quantum dots although it was previously a difficult task.[39–43] Thereby the efficient spin filtering can be exploited by modifying the Rashba spin–orbit-coupling effect under an AC bias to induce a $\pm\pi/2$ phase factor.

The spin-dependent average current response as a function of DC bias voltage $V_{DC} = \mu_L - \mu_R$ is simulated in Fig. 7. Under the synchronous phase factors ($\psi = \Delta\phi_R$) induced by the Rashba spin–orbit-coupling and magnetic flux, the $\langle I\rangle$–V_{DC} curves generally display multiple-step response for spin up/down electrons, as illustrated in Fig. 7(a). It is associated with the occurrence of a series of sideband resonance peaks with different photon-assisted tunneling processes. It is found that the spin polarization is enhanced with the increase of the DC bias voltage. The direction of spin polarization is reversed by applying a polarity reversal DC bias. It is important to point out that the synchronous phases of $\psi = \Delta\phi_R$ for spin up electrons (spin index $\sigma = 1$) lead to the zero phase factor ($\psi - \sigma\Delta\phi_R = 0$) in the matrix elements of Eq. (6). This causes complete degenerate electron transport of the spin up state to produce the same average current characteristics in the $\langle I\rangle$–V_{DC} diagram, as plotted by the solid line in Fig. 7(a).

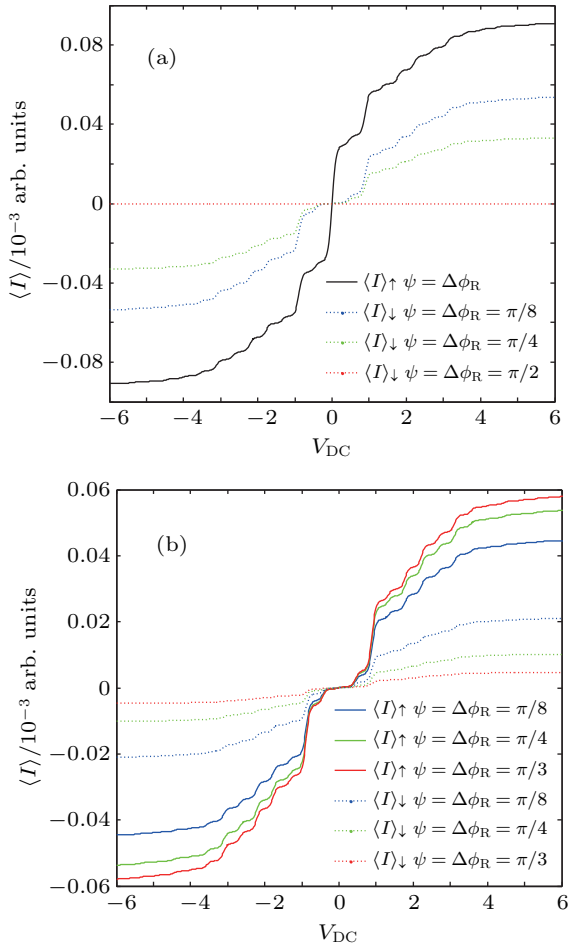


Fig. 7. (color online) Spin-dependent average currents $\langle I\rangle_\uparrow$ (solid line) and $\langle I\rangle_\downarrow$ (dotted line) versus DC bias V_{DC} under a symmetric time-dependent external field ($W_{L(R)} = \omega = 1.0$). The parameters are $k = 2.0$, $\varepsilon_d = 0$ with (a) $\psi = \Delta\phi_R = \pi/8$ (blue curve), $\psi = \Delta\phi_R = \pi/4$ (green curve), $\psi = \Delta\phi_R = \pi/2$ (red curve) and (b) $\Delta\phi_R = \pi/8$ (black curve), $\Delta\phi_R = \pi/4$ (green curve), $\Delta\phi_R = \pi/3$ (red curve), $\psi = \pi/2$.

However, for spin down electrons with the synchronous phase factors of $\psi = \Delta\phi_{\rm R} = \pi/8$, $\pi/4$, $\pi/2$, the average current amplitudes are overall reduced with the increase of the Rashba spin–orbit-coupling induced phase $\Delta\phi_{\rm R}$. At the critical phase of $\psi = \Delta\phi_{\rm R} = \pi/2$, the zero amplitude of the $\langle I\rangle$–$V_{\rm DC}$ curve is obtained for spin down electrons ($\sigma = -1$). Thereby an efficient strategy of a spin sieve purifier can be suggested in principle by electronically manipulating the synchronous phase factors of $\psi = \Delta\phi_{\rm R} = \pi/2$ under a DC bias.

It is worthwhile pointing out that the spin down average current versus magnetic flux becomes π-periodic under the synchronous phase condition of $\psi = \Delta\phi_{\rm R}$. With further increasing magnetic flux in the range of $\pi/2 < \psi\,(= \Delta\phi_{\rm R}) < \pi$, the average current amplitude increases but the direction of the spin down current remains unchanged. Accordingly, it is concluded that the direction and amplitude of the spin polarization can be regulated by tuning the DC bias and the synchronous phase factors induced by the magnetic flux and Rashba spin–orbit-coupling, under a symmetrically time-modulated external field.

Figure 7(b) illustrates the effect of the Rashba spin–orbit-coupling-induced phase factor ($\Delta\phi_{\rm R}$) on the spin-dependent average current when the magnetic flux induced phase is fixed at $\psi = \pi/2$. With the increase of the phase factor $\Delta\phi_{\rm R}$ in the range of 0–$\pi/2$, the spin up average current increases; however, the spin down average current decreases. Thus, the magnitude of the spin polarized current in the model system can be controlled via the Rashba spin–orbit coupling strength by varying the strength of the electric field applied in the experiment.

Figure 8 demonstrates the role of different quantum dot structures on the average current resonance response under an asymmetrical external field. The simulation results at $k_{1,2} = 0$, $k_2 = 0 \& k_1 \neq 0$, and $k_{1,2} \neq 0$ represent the cases in which a single quantum dot, a double-quantum dot molecule, and a triple-quantum dot molecule are inserted into the two arms of the A–B interferometer, respectively. For the single quantum dot structure ($k_{1,2} = 0$), a negative current resonance dip takes place close to the positive main resonant peak, as shown by the solid line in Fig. 8. The negative current is caused by the electron-photon pump effect.[36] When the energy level is lower than $\mu_{\rm L}$, it can be occupied by one electron. Under the time-dependent field, the electron can absorb a photon and tunnel into the left lead but not to the right lead, since the field is only applied on the left lead. This results in a negative current. Moreover, in the absence of the time-dependent field, a new tunneling channel forms when two additional side-couple quantum dots couple with the quantum dots in each arm of the A–B interferometer, respectively. This causes the two (three) main resonance peaks to appear in the average current curves of the double (triple)-quantum dot molecule A–B interferometer. If the time-dependent field is introduced, the photon-assisted sideband peaks are produced. Under the asymmetrical external field, two (three) electron-photon pump phenomena can be observed in the average current curve of the double (triple)-quantum dot molecule A–B interferometer, as shown by the dashed and dotted lines in Fig. 8. These are due to the photonic sidebands induced by the time-dependent field. It is predicted that more electron-photon pump regimes can be exploited when multi-quantum dot molecules are designed to construct a complex A–B interferometer device.

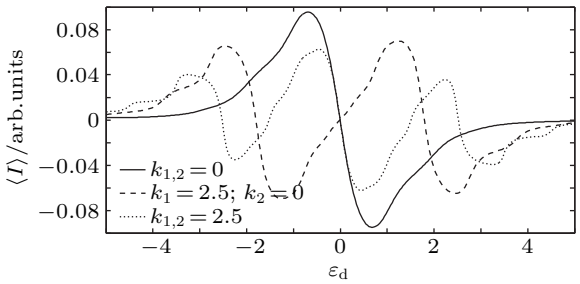


Fig. 8. Average current spectra of different quantum dot structures under an asymmetric external field. The parameters are $W_{\rm L} = 1.0$, $W_{\rm R} = 0$, $\omega = 1.0$, $\Delta\phi_{\rm R} = 0$, and $\psi = 0$.

4. Conclusion

We have theoretically investigated the photon-assisted electronic and spin transport properties through a T-shaped three-quantum-dot molecule A–B interferometer. The time-modulated quantum transport properties have been analyzed under a time-dependent external field by employing the Keldysh non-equilibrium Green's function technique. With the time-dependent external field, the photon-assisted average current spectra exhibit a remarkable sideband effect. The magnitude and position of the average current resonance peaks can be regulated by varying the interdot coupling strength and the amplitude of the time-dependent external field. A strong A–B effect of the average current is present when a magnetic flux is introduced into the multi-quantum dot molecules system. Pure spin-up (or spin-down) polarized transmission is achievable in the whole quantum dot energy region by tuning the Rashba spin orbit coupling strength. A multiple-step quantized profile of the $\langle I\rangle$–$V_{\rm DC}$ curves is obtained in the numerical simulation. It is found that the direction and magnitude of the spin polarization can be controlled by tuning the DC bias, magnetic flux- and Rashba spin–orbit-coupling-induced phase factors in the symmetric AC field. The electron-photon pump function is exploited under a time-modulated asymmetric external field.

References

[1] Hanson R and Awschalom D D 2008 *Nature* **453** 1043
[2] Kondo K 2016 *New J. Phys.* **18** 013002
[3] Bragar I and Cywinski L 2015 *Phys. Rev. B* **91** 155310
[4] Loss D and DiVincenzo D P 1998 *Phys. Rev. A* **57** 120
[5] DiVincenzo D P 2005 *Science* **309** 2173

[6] Lovett B W, Reina J H, Nazir A and Briggs G A D 2003 *Phys. Rev. B* **68** 205319
[7] Petta J R, Johnson A C, Taylor J M, Laird E A, Yacoby A, Lukin M D, Marcus C M, Hanson M P and Gossard A C 2005 *Science* **309** 2180
[8] He Z L, Bai J Y, Li P and Lü T Q 2014 *Acta Phys. Sin.* **63** 227304 (in Chinese)
[9] Bai J Y, He Z L and Yang S B 2014 *Acta Phys. Sin.* **63** 017303 (in Chinese)
[10] He Z L, Lü T Q, C L, Xue H J, Li L J and Yin H T 2011 *Chin. Phys. B* **20** 117303
[11] Bai J Y, He Z L, Li L, Ye S J and Sun W M 2017 *Physica B* **521** 148
[12] He Z L, Bai J Y, Ye S J, Li L and Li C X 2017 *Chin. Phys. Lett.* **34** 087301
[13] Vasseur R and Moore J E 2014 *Phys. Rev. Lett.* **112** 146804
[14] Beltukov Y M and Greshnov A A 2015 *Semiconductors* **49** 483
[15] Piotr T 2010 *Phys. Rev. B* **82** 125323
[16] Wójcik K P and Weymann I 2015 *Phys. Rev. B* **91** 134422
[17] Zhao H K and Zou W K 2015 *Phys. Lett. A* **379** 389
[18] Xu W P, Zhang Y Y, Wang Q, Li Z J and Nie Y H 2015 *Phys. Lett. A* **380** 958
[19] Koch T, Loos J and Fehske H 2014 *Phys. Rev. B* **89** 155133
[20] Zhao X, Yuan R Y, Ji A C, Yan H and Guo Y 2014 *J. Appl. Phys.* **116** 103517
[21] Wójcik K P and Weymann I 2014 *Phys. Rev. B* **90** 115308
[22] Žitko R 2010 *Phys. Rev. B* **81** 115316
[23] Zeng Q B, Chen S and Rong L 2016 *Phys. Lett. A* **380** 951
[24] Mavalankar A, Pei T, Gauger E M, Warner J H, Briggs G A D and Laird E A 2016 *Phys. Rev. B* **93** 235428
[25] Hohenester U, Laucht A, Kaniber M, Hauke N, Neumann A, Mohtashami A, Seliger M, Bichler M and Finley J J 2009 *Phys. Rev. B* **80** 201311
[26] Oosterkamp T H, Kouwenhoven L P, Koolen A E A, van der Vaart N C and Harmans C J P M 1996 *Semicond. Sci. Technol.* **11** 1512
[27] Qin H, Holleitner A W, Eberl K and Blick R H 2001 *Phys. Rev. B* **64** 241302
[28] Sun Q F, Wang J and Lin T H 1998 *Phys. Rev. B* **58** 13007
[29] Oosterkamp T H, Kouwenhoven L P, Koolen A E A, van der Vaart N C and Harmans C J P M 1997 *Phys. Rev. Lett.* **78** 1536
[30] Shibata K, Umeno A, Cha K M and Hirakawa K 2012 *Phys. Rev. Lett.* **109** 077401
[31] You J, Li H O, Cao G, Deng G W, Xiao M and Guo G P 2015 *Europhys. Lett.* **111** 17001
[32] Zhao H K, Zou W K and Chen Q 2014 *J. Appl. Phys.* **116** 093702
[33] Zhao H K and Zhao L L 2011 *Europhys. Lett.* **93** 28004
[34] Zhao H K, Zhang J and Wang J 2015 *Europhys. Lett.* **109** 18003
[35] Tang H Z, An X T, Wang A K and Liu J J 2014 *J. Appl. Phys.* **116** 063708
[36] Sun Q F and Lin T H 1997 *Phys. Rev. B* **56** 3591
[37] Wingreen N S, Jauho A. P and Meir Y 1993 *Phys. Rev. B* **48** 8487
[38] Jauho A P, Wingreen N S and Meir Y 1994 *Phys. Rev. B* **50** 5528
[39] Sun Q F, Wang J and Guo H 2005 *Phys. Rev. B* **71** 165310
[40] Sun Q F and Xie X C 2006 *Phys. Rev. B* **73** 235301
[41] Nitta J, Akazaki T, Takayanagi H and Enoki T 1997 *Phys. Rev. Lett.* **78** 1335
[42] Grundler D 2000 *Phys. Rev. Lett.* **84** 6074
[43] Mireles F and Kirczenow G 2001 *Phys. Rev. B* **64** 024426